Self-sustained instability, transition, and turbulence induced by a long separation bubble in the footprint of an internal solitary wave. II. Flow statistics

Takahiro Sakai **

Department of Aerospace and Mechanical Engineering, University of Southern California, California 90089-1191, USA

Peter J. Diamessis @

School of Civil and Environmental Engineering, Cornell University, Ithaca, New York 14853, USA

Gustaaf B. Jacobs

Department of Aerospace Engineering, San Diego State University, San Diego, California 92182, USA

(Received 26 February 2020; accepted 22 September 2020; published 28 October 2020)

The statistical properties of the self-sustained turbulent wake downstream of a long, high-aspect-ratio, laminar separation bubble are studied. The primary focus is on the relaxation of turbulent wake to a zero pressure gradient (ZPG) turbulent boundary layer, in terms of mean flow, Reynolds stresses, and turbulent kinetic energy (TKE) budget. The bubble is initiated by the strong adverse pressure gradient (APG) induced by a large-amplitude, laboratory-scale internal solitary wave of depression propagating against an oncoming barotropic current. The high-resolution large eddy simulation data generated in Part I of this two-part article is used for analysis. It is shown that the wake development in the early stage, following the breakdown of coherent vortices toward the trailing region of the separation bubble, possesses a statistical character similar to that of a self-similar plane mixing layer. The mean streamwise velocity profile relaxes to that of a ZPG turbulent boundary layer at 15 water column depths form the wave trough. This relaxation distance normalized by the bubble length is equal to 5 which is shorter than reported by Alam and Sandham's short bubble [J. Fluid Mech. 403, 223 (2000)] that is induced by a stronger APG. In regions further downstream of the bubble, distributions of the Reynolds stresses resemble those of channel flow. The relaxation of the TKE budget to that of a ZPG turbulent boundary layer is slower far away from the wall and faster near the wall, as compared to the relaxation of the mean flow to that of a ZPG turbulent boundary layer. Large bed stresses beneath the shed vortices and persistent near-bed turbulence offer an insight into frequently observed sediment resuspension events in coastal seas.

DOI: 10.1103/PhysRevFluids.5.103802

I. INTRODUCTION

In Part I of this two-part paper, we performed a highly resolved, implicit large eddy simulation (LES) to simulate the bottom boundary layer (BBL) induced by an internal solitary wave (ISW) propagating against an oncoming, quiescent barotropic current at laboratory scale. We reproduced

^{*}tsakai@usc.edu

a self-excited and self-sustained bottom turbulent wake over a long domain. It was shown that the oncoming barotropic current effectively induces a separation bubble in the wave's footprint, where a three-dimensional (3D) global instability [1] is excited. The separation bubble continually sheds a train of Kelvin-Helmholz–type vortices that subsequently degenerate into smaller scales of motion through an elliptic instability [2] and short-wave instabilities, eventually yielding an energetic turbulent wake downstream. The topological evolution of this flow described in Part I forms the basis for the statistical analysis presented in this Part II.

The resulting separation bubble has a substantially higher aspect ratio, $h_b/l_b \approx 85$ (l_b is the length and h_h is the maximum height of the bubble, measured from the mean separating streamline), relative to those observed in aerodynamic studies such as the cases investigated by Alam and Sandham [3] (\approx 26 and 43), Diwan and Ramesh [4] (\approx 24) and Marxen and Henningson [5] (\approx 21, 26, and 33), among many others. For these short bubbles, generally, an oncoming laminar boundary layer forced with weak disturbances undergoes separation driven by a local upper-wall suction (or deformed upper wall), leading to transition to turbulence and reattachment. In our case, a perturbation-free background current modeled by a Blasius boundary layer interacts with a large-scale, ISW-induced current field, forming a long, laminar separation bubble whose length is comparable with the ISW wavelength. Transition mechanisms of shorter separation bubbles are most often driven by an extrinsic, forcing-dependent convective instability of the separated shear layer [4,6,7], as opposed to the intrinsically driven global instability [8] (Part I). The short separation bubbles strongly amplify instabilities in the separated flow which causes an early transition to turbulence near the trailing edge of the bubble, still upstream of the flow reattachment point [9,10]. For a long separation bubble, in contrast, the BBL flow remains essentially 2D up to about half a bubble length downstream of the trailing edge of the bubble.

Statistical properties of the wake and wall-bounded flow downstream of the canonical short bubbles have been documented by Alam and Sandham [3] and Spalart and Strelets [11]. Alam and Sandham's direct numerical simulations (DNS) showed that the turbulent wake initially has a statistical character similar to that of a self-similar plane mixing layer and that it then gradually relaxes to a zero pressure gradient (ZPG) turbulent boundary layer further downstream. In the context of the ISW-induced BBL, we observe a similar series of characteristic flow states that have a footprint along the bed until the flow relaxes to a nominal turbulent boundary layer, including the early stage of vortex shedding and the energetic turbulence driven by the vortex breakdown and its associated mixing-layer-like flow. These stages can also be interpreted as a "memory" or a "signature" of the wave-induced adverse pressure gradient (APG).

Two critical questions which remain to be answered, in view of coastal applications such as continental shelf energetics and sediment transport, are as follows: (a) whether or not a wake relaxation or a "loss of memory" of the APG occurs in a manner similar to the case of the shorter separation bubble and (b) how quickly the memory of the APG is "forgotten" in the lee of an ISW-induced long separation bubble, in terms of mean and turbulent flow quantities and as a function of bed-normal distance. Ultimately, the answers to these questions provide useful insights and a database to aid turbulence modeling of ISW-induced BBLs for the efficient forecasting of "weather" of coastal boundary layers. Such a study is also of interest to more general readers studying laminar-to-turbulent transition: Predominantly the aerodynamics community has extensively explored the short separation bubble case, as per the representative studies illustrated above.

This paper aims to explore the spatial development and relaxation of the ISW-induced bottom turbulent wake, both in the streamwise and bed-normal directions, by characterizing the flow in terms of its mean and turbulent fluctuations, with extensive emphasis of the latter. To understand the development and relaxation of the ISW-induced wake, the 3D data set obtained in Part I is analyzed. In Sec. II, we describe the numerical model and basic structure of the BBL flow, providing only limited information that is required to interpret the results presented in this report. The reader familiar with Part I of this study may skip this section. In Sec. III A, mean flow properties are discussed and offer a quantitative overview of the spatial development of the BBL. It is found that the streamwise velocity profile approaches that of ZPG after 15 water column depths downstream

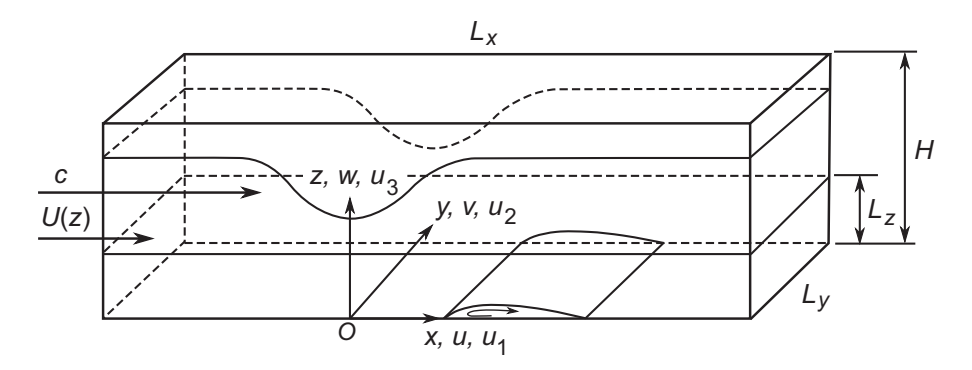


FIG. 1. Schematic diagram of physical model. The frame of reference is fixed to the wave propagating leftward (negative x direction). In the wave-fixed reference frame, in addition to the background barotropic current, one experiences a uniform current c oriented in the left-to-right x direction.

from the wave trough. This relaxation distance normalized by the bubble length is shorter than the case of Alam and Sandham's short bubble [3] that is driven by a stronger APG. Presentation of the spatial development of Reynolds stresses and turbulent kinetic energy (TKE) budgets follows, in Sec. III B and Sec. III C, respectively, with comparison to available DNS results of series of canonical turbulent flows. It is found that the intense turbulence produced by vigorous vortex shedding, i.e., a memory of APG, persists for a long downstream distance, as manifested by the slower relaxation of turbulent fluctuations in the far-wall region and faster relaxation of the same quantities in the viscous-wall region, relative to the relaxation distance of the mean flow to a ZPG turbulent boundary layer. In Sec. IV, we will discuss the implications of such energetic bottom turbulence for episodic sediment resuspension (a visible signature of the APG), as well as for the potential relevance of laboratory-scale models to field observations.

II. DESCRIPTION OF FLOW MODEL

A. Numerical model

This section summarizes the numerical model and setup. For a complete description, the reader is referred to Part I. The physical domain is a 3D rectangular channel located in a frame of reference fixed to an ISW of depression propagating in the negative x direction with speed c against the oncoming background current U(z) (Fig. 1). The wave is supported by a continuous, two-layer density stratification with the pycnocline depth at $z_0 = 13H/15$ with the thickness d = H/15, where H is the water column depth. The background current U(z) is a model-parallel flow with a magnitude $U_0 = 0.5c_{w0}$, where $c_{w0} = c + U_0$. U(z) has a Blasius profile across the bottom 5% of the water column depth. The present wave, having the amplitude 0.346H and the wavelength $\lambda_w = 2.33H$, is a solution to the Dubriel-Jacotin-Long (DJL) equation [12]. The wave Reynolds number is $Re_w = 1.6 \times 10^5$, defined as $Re_w = c_{w0}H/v$, where v is the kinematic viscosity.

The height-reduced computational domain, intended to alleviate the significant computational cost, has dimensions $L_x \times L_y \times L_z = 26H \times 0.15H \times 0.3H$. The reduced height computational domain is unstratified, as only the lower layer of the water column is contained therein. The coordinate origin (on the wave center line) is set at a 6H along-bottom distance away from the inflow boundary.

The flow field (\mathbf{u}, p) is governed by the incompressible Navier-Stokes equations formulated such that the ISW-induced field and U(z) are forced to be fixed in time. The computational domain is set to be periodic in the horizontal x and y directions with a sponge layer of thickness H at the inflow and outflow boundary of the domain to produce a disturbance-free inflow state. The no-slip boundary

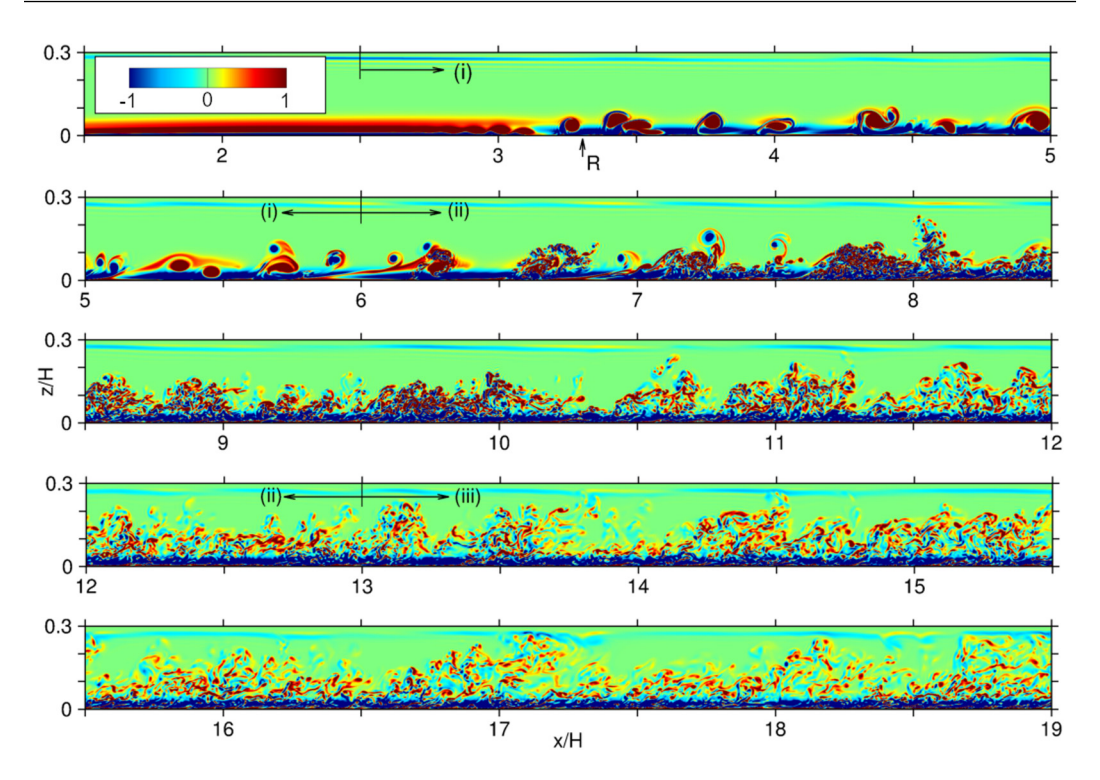


FIG. 2. Spatial development of instantaneous spanwise perturbation vorticity $\omega_y \delta_s/c_{w0}$ over 1.5 < x/H < 19 split equally. Each window has a length of $1.5\lambda_w$. The flow domain is categorized roughly into the three regimes: (i) two- and three-dimensional instability and transition: 2.5 < x/H < 6 ($1.1 < x/\lambda_w < 2.6$); (ii) vortex breakup and formation of turbulent clouds: 6 < x/H < 13 ($2.6 < x/\lambda_w < 5.6$); (iii) developing turbulent boundary layer: x/H > 13 ($x/\lambda_w > 5.6$). The symbol x together with an arrow in the top panel indicate the mean flow reattachment point.

condition is applied along z = 0, and a stress-free condition together with a thin (0.025H) sponge layer are applied along the top surface (z = 0.3H).

The field equation is numerically integrated with the parallel flow solver presented in [13] and is based on a spectral multidomain penalty method in the vertical z and Fourier discretization in the x and y directions. An exponential spectral filter applied in all directions at every time step ensures stability of the solver. No explicit wall model is employed.

The grid resolution is $N_x \times N_y \times N_z = 12\,288 \times 128 \times 480$ (\$\approx 750\$ million points) with the mesh size in wall units equal to $\Delta x^+ = 8.2$, $\Delta y^+ = 4.6$, and $\Delta z^+ = 0.027$ (at z = 0). There are 18 vertical grid points within the viscous sublayer ($z^+ < 5$) and 123 points within the viscous wall region ($z^+ < 50$). The model is simulated for $0 < t < 9.0 \lambda_w/c$ ($c = 0.5 c_{w0}$) and the last 1/3 of integration time is spent for time averaging.

B. Spatial development of flow structure

To connect the statistical results to the development of flow structures, a representative contour of instantaneous spanwise vorticity is plotted in Fig. 2 (the same as Fig. 7 in Part I), which we will use as an illustrative reference of the spatial development of flow structure of the wave-induced BBL. The flow separation location is upstream of the visualization window, at x = 0.602H; the mean flow reattachment point is at x = 3.304H; the bubble length is thus $l_b = 2.702H$ (the figure visualization window covers a downstream distance of about $6l_b$ from the flow reattachment location). As discussed in detail in Part I, the flow structure can be categorized into three regimes, comprising

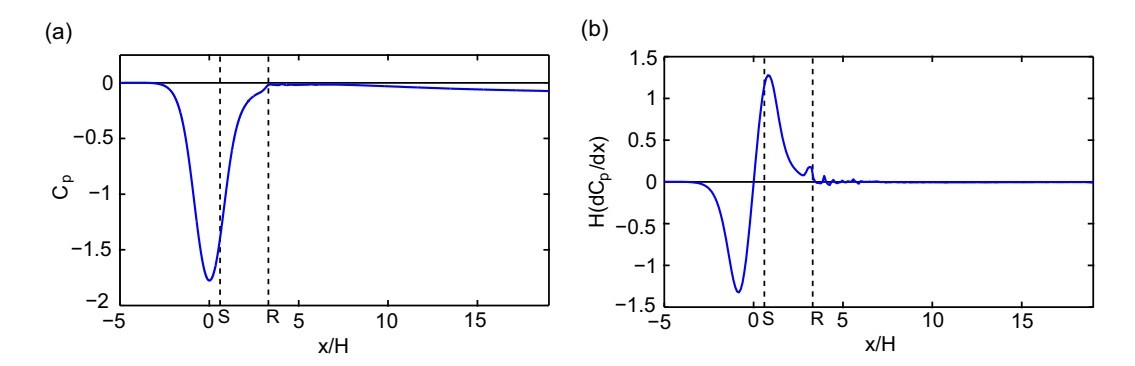


FIG. 3. (a) Streamwise variations of the time-averaged pressure coefficient along the bottom boundary and (b) the corresponding dimensionless pressure gradient along the bottom, $H(dC_p/dx)$. The streamwise location of the flow separation point is marked by the symbol S, and that of the mean flow reattachment point is marked by R, along with vertical dashed lines for both.

(i) 2.5 < x/H < 6 ($1.1 < x/\lambda_w < 2.6$), representing the 3D global instability and transition, where vortex shedding, subsequently pairing, merger and bending driven by the elliptic instability occur; (ii) 6 < x/H < 13 ($2.6 < x/\lambda_w < 5.6$), representing the vortex breakup and turbulent cloud formation, where the shortwave secondary instability, in the form of streamwise vortex streaks, quickly disintegrates the merged vortices into smaller scales of motion, forming clouds of turbulent eddies; and (iii) x/H > 13 ($x/\lambda_w > 5.6$), representing the spatially developing turbulent boundary layer, in which the (large) coherent structure in the train of shed vortices breaks up and is nearly lost. The regime (ii) is associated with a mixing layer state, and the regime (iii) is linked to an equilibrium turbulent boundary layer. These regimes are similar to what was observed by Alam and Sandham [3] in the wake behind their short bubble. In Secs. III B and III C we will show that these regimes can also be identified in the flow relaxation behind a long separation bubble.

III. RESULTS

A. Mean flow properties

In this section, we explore the mean flow quantities to characterize the flow in terms of APG, boundary layer profile, and bottom friction coefficient. We compare the results with those of canonical short bubbles and ZPG turbulent boundary layers with the intent of quantifying the relaxation of the turbulent wake to a ZPG turbulent boundary layer and to identify similarities and differences in the nature of relaxation our long bubble and representative short bubbles.

Figure 3 shows the pressure coefficient and the nondimensional pressure gradient calculated along the bottom boundary. The pressure coefficient is defined as $C_p = 2(\overline{p} - p_0)/\rho_0 c_{w0}^2$, where \overline{p} is the pressure averaged in time and span and p_0 is the pressure of the undisturbed flow upstream of the wave. In the figure, locations of the mean flow separation point (symbol S) and the mean reattachment point (symbol R), defined as the positions at which the mean bottom shear stress vanishes, are also indicated.

The APG region extends from the wave trough to the flow reattachment point. The maximum APG scaled by the bubble length is $l_b(dC_p/dx)_{\rm max}=0.34$, which is weaker than what is found in the cases of typical short bubbles such as ≈ 0.43 (Alam and Sandham [3]), ≈ 1.35 (Spalart and Strelets [11]), and ≈ 0.79 (Le *et al.* [14] for the backward facing step).

After the reattachment, the pressure gradient changes to a very weak, favorable pressure gradient (FPG) that continues toward the downstream end of the domain. This FPG is two orders of magnitude smaller than the maximum APG near the flow separation point. A FPG region in the flow downstream of a short separation bubble is also reported in DNS results by Spalart and Strelets

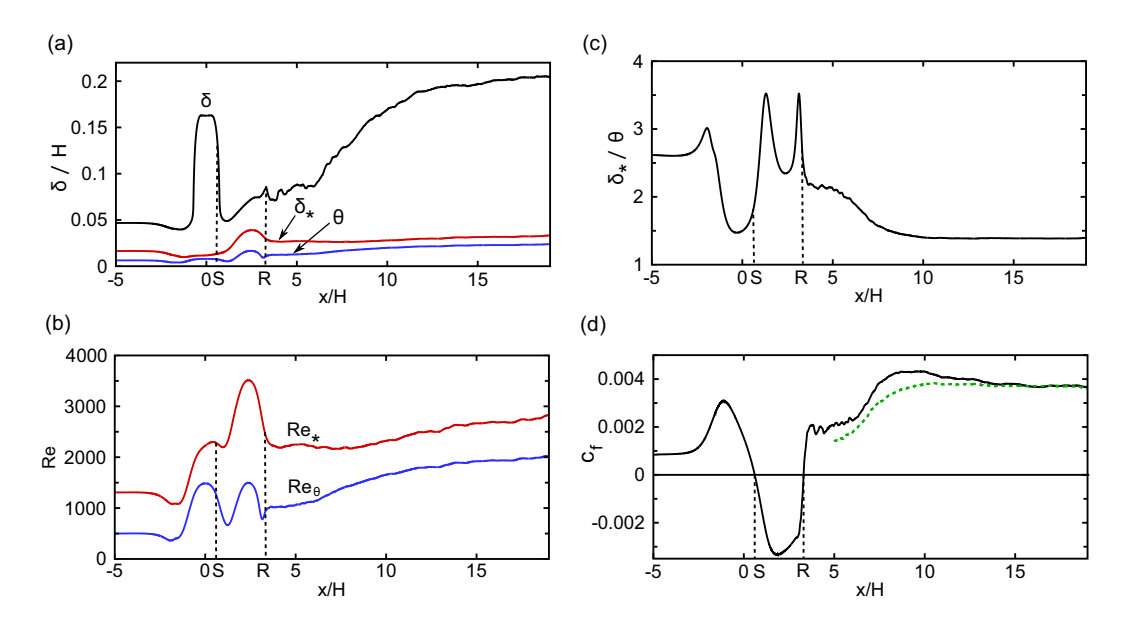


FIG. 4. (a) Boundary layer thickness δ_t , displacement thickness δ_t , and momentum thickness δ_t ; (b) displacement thickness Reynolds number Re_t and momentum thickness Reynolds number Re_t ; (c) shape factor δ_t/θ ; and (d) skin friction coefficient c_f together with the Ludwieg-Tillman correlation in dashed curve, all as functions of the streamwise coordinate x. Vertical dashed lines indicate the separation point (S) and reattachment point (S). The wavelength is $\delta_t = 2.33H$.

[11] and Alam and Sandham [3]. Spalart and Strelets attributed this FPG, although very weak, to the presence of the free-slip upper wall (to enable domain truncation).

Figure 4 shows the spatial development of the boundary layer thickness δ , displacement thickness δ_* , momentum thickness θ and the corresponding thickness-based Reynolds numbers $\mathrm{Re}_* = (u_\infty - c)\delta_*/v$ and $\mathrm{Re}_\theta = (u_\infty - c)\theta/v$, respectively. u_∞ is the local free stream velocity based on the mean streamwise velocity \overline{u} . The boundary layer thickness δ is defined as the vertical offset at which $(\overline{u} - c)$ equals $0.99(u_\infty - c)$. The displacement and momentum thicknesses are defined as

$$\delta_* = \int_0^\delta \left(1 - \frac{\overline{u} - c}{u_\infty - c} \right) dz \quad \text{and} \quad \theta = \int_0^\delta \frac{\overline{u} - c}{u_\infty - c} \left(1 - \frac{\overline{u} - c}{u_\infty - c} \right) dz. \tag{1}$$

Also shown are the shape factor δ_*/θ and the bottom skin friction coefficient defined as $c_f = 2\tau_b/\rho_0(u_\infty - c)^2$.

The large boundary layer thickness δ at the wave trough observed in Fig. 4(a) is attributed to a weak vertical shear of the wave-induced, inviscid steamwise velocity, although such a large δ does not sufficiently contribute to the increase of the values of δ_* because the vertical shear is much smaller as compared to the shear at the wall vicinity. The displacement thickness ratio relative to the boundary layer thickness at the developing turbulent boundary layer stage (iii) is $\delta_*/\delta \approx 0.16$, and the corresponding value of a nominal ZPG turbulent boundary layer is $\delta_*/\delta \approx 1/8 = 0.125$ (e.g., see Ref. [15]). The momentum thickness ratio relative to the boundary layer thickness at the developing stage is $\theta/\delta \approx 0.116$, which is comparable in magnitude to $\theta/\delta \approx 7/72 = 0.097$ of a nominal ZPG turbulent boundary layer [15].

Figure 4(c) shows that the shape factor δ_*/θ decreases to nearly a constant value of 1.38 after $x \approx 10H$ ($\approx 4.3\lambda_w$). According to Coles' empirical correlations [16] for an incompressible ZPG flat plate turbulent boundary layers, $\delta_*/\theta = 1.405$ for $\text{Re}_\theta = 2050$. The correlation formulated by Monkewitz *et al.* [17] gives $\delta_*/\theta \approx 1.42$ near the downstream end of the domain. The corresponding

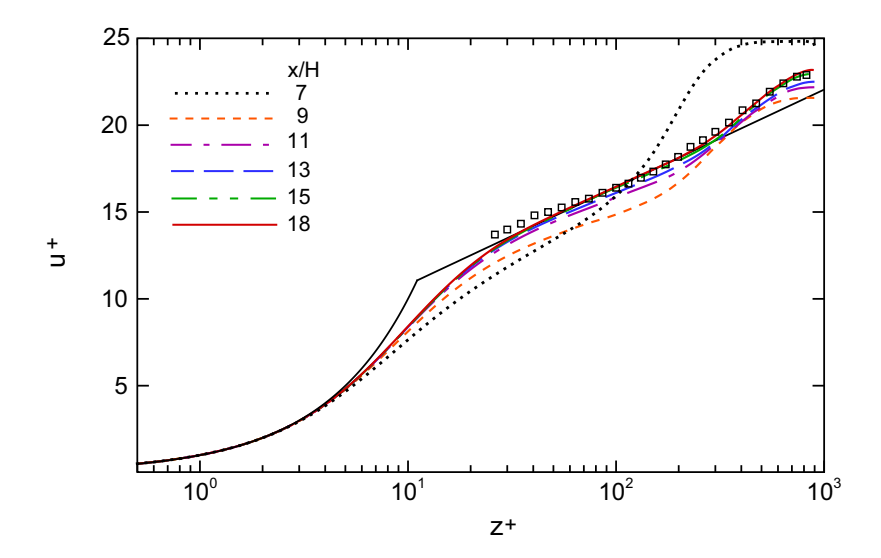


FIG. 5. Streamwise velocity profile in wall-scaled coordinates for different streamwise locations together with Murlis *et al.* [21] at Re_{θ} = 1900 (\square), viscous-wall law $u^+ = z^+$ (black solid for $z^+ < 10$), and log law of the wall $u^+ = \frac{1}{0.41} \log z^+ + 5.2$ (black solid for $z^+ > 10$). $u^+ \equiv (\overline{u} - c)/u_\tau$, where u_τ is the local friction velocity defined as $u_\tau \equiv \sqrt{\tau_b/\rho_0}$. $z^+ \equiv zu_\tau/v$.

shape factor value of the present case $(\delta_*/\theta = 1.38)$ is slightly less than these benchmark problem values. This discrepancy is attributed to the effect of weak downstream FPG.

Figure 4(d) shows that the skin friction coefficient increases rapidly in the vortex breakup and turbulent cloud formation region. After reaching the maximum value $c_{f\text{max}} = 0.00433$ at x = 9.5H ($\approx 4.1 \lambda_w$), it gradually decreases and its value virtually settles to nearly a constant value of $c_f \approx 0.0037$. In the same figure, the commonly used empirical value of Ludwieg-Tillman skin friction [18], i.e., $c_f = 0.246 \times 10^{-0.678 \delta_*/\theta} [(u_\infty - c)\theta/\nu]^{-0.268}$, is also plotted for comparison. An excellent agreement is observed for x > 15H ($\approx 6.4 \lambda_w$).

In Fig. 5, wall-scaled streamwise velocity profiles u^+ are shown for several different streamwise locations from x = 7H ($\approx 3\lambda_w$) to x = 18H ($\approx 7.7\lambda_w$). Here the velocity scale is the friction velocity $u_\tau \equiv \sqrt{\tau_b/\rho_0}$, and the viscous wall length scale is $l_\tau \equiv v/u_\tau$. Excellent agreement with the viscous-wall law is observed in all streamwise locations. In the near wall region, the velocity profiles approach the log law of the wall downstream of the wave. A slight downward deviation from the log-law is observed similarly to the cases of Alam and Sandham's short bubble and Le *et al.*'s backward-facing step [14], which is a common trend in turbulent boundary layer flows that experience a strong APG (cf. Nagano *et al.* [19] and Monty *et al.* [20] among others). The velocity profiles are almost identical beyond x = 15H ($\approx 6.4\lambda_w$). In the same figure, experimental data of a ZPG flat plate boundary layer extracted from Murlis *et al.* [21] for Re_{\theta} = 1900 is included. An excellent agreement is observed beyond the log-law region for the simulated flow profiles at x = 15H. This observation suggests that the mean flow, at least, has lost the "memory" of wave-induced APG by $x \approx 15H$. As will be shown in Secs. III B and III C, this loss of memory is nuanced when considered in the context of turbulent quantities.

Summarizing, the results in this section verify the claim that the wake relaxation to a ZPG turbulent boundary layer, observed in the Alam and Sandham's short separation bubbles typical in aerodynamic flows, is also occurring downstream of the ISW-induced long separation bubble. The aspect ratios of Alam and Sandham's short bubbles are approximately 43 (case 3DF-A) and 26 (case 3DF-B) compared to 85 of our long bubble. The streamwise-velocity profile, shape factor, and bed friction coefficient suggest that the relaxation distance to the ZPG turbulent boundary layer

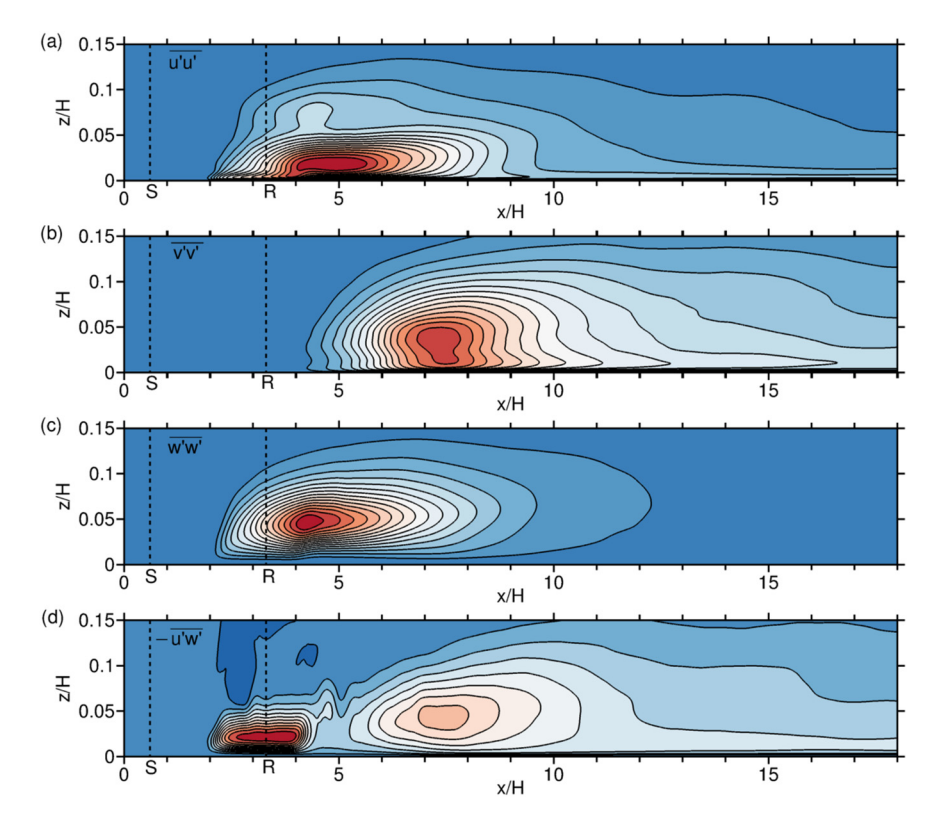


FIG. 6. Spatial distribution of Reynolds stresses. All the stresses are scaled by the maximum along-bed stress $u_{\tau_{\text{max}}}^2$. (a) $\overline{u'u'}$: fifteen contour levels from 2.0 (blue) to 30.0 (red), equally spaced. (b) $\overline{v'v'}$: fifteen contour levels from 0.333 (blue) to 5.0 (red), equally spaced. (c) $\overline{w'w'}$: fifteen contour levels from 1.67 (blue) to 25 (red), equally spaced. (d) $-\overline{u'w'}$: eleven contour levels from 0.001 (blue) to 2.5 (red), equally spaced. x coordinates of separation (x) and reattachment (x) are indicated by dashed lines.

is about $15H \approx 6.5\lambda_w$ downstream from the ISW trough. This relaxation distance corresponds to about $5l_b$ from the flow reattachment point.

In Alam and Sandham's case, the relaxation distance is measured at about $6l_b$, longer than our case in term of distance normalized by the bubble length (l_b) . This can be attributed to the strong APG discussed earlier in this section, extending beyond the separation bubble, about one or two bubble lengths downstream of the bubble trailing edge (see their Fig. 5 in Ref. [3]). Such a strong APG in Alam and Sandham's short bubbles is expected to delay the recovery toward a ZPG turbulent boundary layer. This observation is also supported by Le *et al.*'s DNS study of turbulent flow over a backward-facing step [14], as illustrated by a slow recovery of the streamwise velocity profile due to high APG overwhelming the flow recirculation region formed behind the step (see their Fig. 18).

B. Turbulence properties: Reynolds stresses

In this section, we discuss the wake relaxation in terms of Reynolds stresses and TKE, and at the end of this section, the relaxation in the near-wall region is compared with the far-wall flow development.

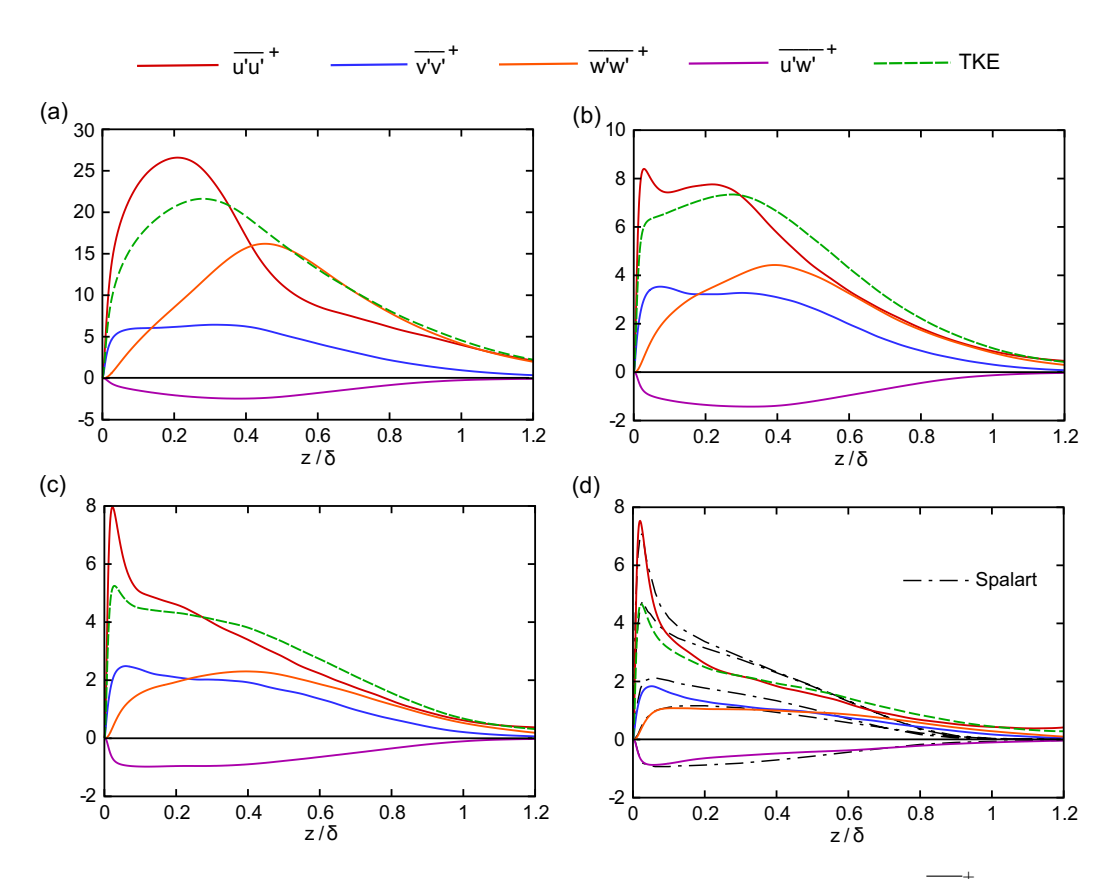


FIG. 7. Wall-normal distribution of Reynolds stresses and turbulence kinetic energy $0.5\overline{u_i'u_i'}^+$ (in dashed line) for different streamwise locations (a) $x = 7H \approx 3\lambda_w$, (b) $x = 9H \approx 3.9\lambda_w$, (c) $x = 11H \approx 4.3\lambda_w$, and (d) $x = 17H \approx 7.3\lambda_w$. Dot-dashed lines in (d) are corresponding stress values computed for ZPG flat-plate boundary layer by Spalart [22] for Re_{\theta} = 1410. All values are scaled by streamwise local value of $u_\tau^2 \equiv \tau_b/\rho_0$. Note the different vertical axis limits across panels.

1. Spatial distribution of Reynolds stresses

In Fig. 6 the spatial development of the Reynolds stresses is plotted. The primed variables denote fluctuating components, and the overbar represents the time and spanwise average. Generally, the Reynolds stresses reduce substantially to only a fraction of their maximum values upstream of the location x = 10H. It is noted that $\overline{u'w'}$ has its maximum value at the mean flow reattachment point where the mean skin friction coefficient is zero. The secondary local maximum is observed at x = 7.5H. At the flow reattachment, the vortex dominated flow is essentially 2D (see Fig. 3 in Part I), which is distinctly different as compared to the short separation bubble of Alam and Sandham. In that flow (case 3DF-A), $\overline{u'w'}$ has only one local maximum at half a bubble length downstream from the reattachment point (see their Fig. 14(e) in Ref. [3]), where the shed vortices are already breaking up and undergo transition to turbulence (see Fig. 12 in Ref. [3]). This early breakup can be attributed to the upstream forcing and the continuous growth of flow perturbations by the instability in the separated shear layer along the bubble. In contrast, our long bubble is unforced, and disturbances are affected only by a global instability whose growth rate may not be strong enough to cause an earlier 3D flow transition. A gentler ISW-induced APG and/or a narrow domain width chosen for the study may be additional factors in the delayed transition.

In Fig. 7, the wall-normal distribution of the Reynolds stresses in local wall units is shown for selected streamwise locations at x = 7H ($\approx 3\lambda_w$), representing a vortex-breakup followed by an early stage of the turbulent cloud formation; x = 9H ($\approx 3.9\lambda_w$), representing an intermediate stage of the turbulent cloud formation; x = 11H ($\approx 4.3\lambda_w$), representing a later stage of the turbulent cloud formation, and x = 17H ($\approx 7.3\lambda_w$), representing a developing turbulent boundary layer.

All stresses are largest at the early turbulent cloud formation stage [Fig. 7(a)], which would suggest that a significant production of TKE occurs in the turbulent cloud. $\overline{w'w'}$ has greater values in the middle region of the boundary layer. This can be attributed to the upward and downward motions of the bubble-shed energetic coherent vortex train. In the intermediate turbulent cloud formation stage [Fig. 7(b)], a new localized peak in $\overline{u'u'}$ appears in the vicinity of the boundary, $z/\delta < 0.1$ (inner layer). At this same location $\overline{w'w'}$ is substantially reduced. This trend continues throughout the remaining turbulent cloud formation stage, and further decrease of all stresses are observed away from the wall, $z/\delta > 0.1$ [Fig. 7(c)].

In Fig. 7(d), the corresponding stresses obtained by Spalart [22] for a ZPG flat plate turbulent boundary layer at the momentum thickness Reynolds number $Re_{\theta} = 1410$ are included for comparison. Except for $\overline{w'w'}$, the stress values in the present case are smaller withen the range $0.1 < z/\delta < 0.6$. The difference amounts roughly to a 25% reduction compared to the values of Spalart boundary layer. For $z/\delta > 0.6$ the present case exhibits larger values with slower decay of all stresses as compared to the Spalart boundary layer.

To understand the cause of the discrepancy with the Spalart boundary layer in the far-wall region $(z/\delta > 0.1)$, we compare the Reynolds stresses with the DNS data for a fully developed turbulent channel flow at $\text{Re}_{\tau}(\equiv u_{\tau}\delta/\nu) = 590$ obtained by Moser *et al.* [23], as shown in Fig. 8. As in our case, the channel flow data has large Reynolds stresses far away from the wall. In the figure, the comparison is made with both the wall and boundary layer scales. The flat plate boundary layers, the Reynolds stresses at the outer edge of the boundary layer of the channel (i.e., the midplane of the channel) are nonzero because turbulence is also developed at the opposite wall and this turbulence accumulates in the center of the channel. The Reynolds stress profiles in the viscous-wall region $(z^+ < 50)$ are essentially the same as those of the flat plate boundary layers [24].

The present case and the channel flow compare quite well for $0 < z^+ < 300 \ (\approx 0.4\delta)$. Both cases also compare reasonably well for $z/\delta > 0.5$ [Fig. 8(b)]. The nonnegligible turbulence in the far-wall region leads to an increased boundary layer thickness beyond what is expected from ZPG turbulent boundary layers. The discrepancy of the Reynolds stresses in the far-wall region [Fig. 7(d)], therefore, is a result of the difference of the boundary layer scaling, δ , which is larger in our case. Note that the turbulent flows of the wake behind a separation bubble and in the channel have disparate origins, as the former develops from vortex shedding from a shear layer and the latter develops from turbulent boundary layer filling out the entire channel. Nonetheless and interestingly so, their developed flow states have similar Reynolds stress distributions.

2. Near-wall distribution of Reynolds stresses

Motivated by the question of wall-normal uniformity of the wake relaxation process across the boundary layer, the stresses presented in Fig. 7 are now plotted in Fig. 9 as functions of viscous-wall coordinates z^+ over the viscous-wall region. As opposed to the far-wall region, variations in the stress profiles are only moderate in the streamwise direction. Particularly, the stresses in the intermediate and late turbulent-cloud formation stages [Figs. 9(b) and 9(c)] already have qualitatively the same shape as those of the developing turbulent boundary layer stage [Fig. 9(d)], despite the remarkable differences observed in the far-wall region [Figs. 7(b)–7(d)]. Also in contrast to the far-wall region, at the developing turbulent boundary layer stage [Fig. 9(d)], the stress values generally compare very well with those of the Spalart boundary layer, although $\overline{v'v'}$ is a bit smaller than that of Spalart over the entire viscous-wall region. These observations suggest that the near-wall viscous relaxation is faster than that in the outer layer ($z^+ > 50$ or $z/\delta > 0.1$). This will be verified in the next section through examinations of TKE budget distributions.

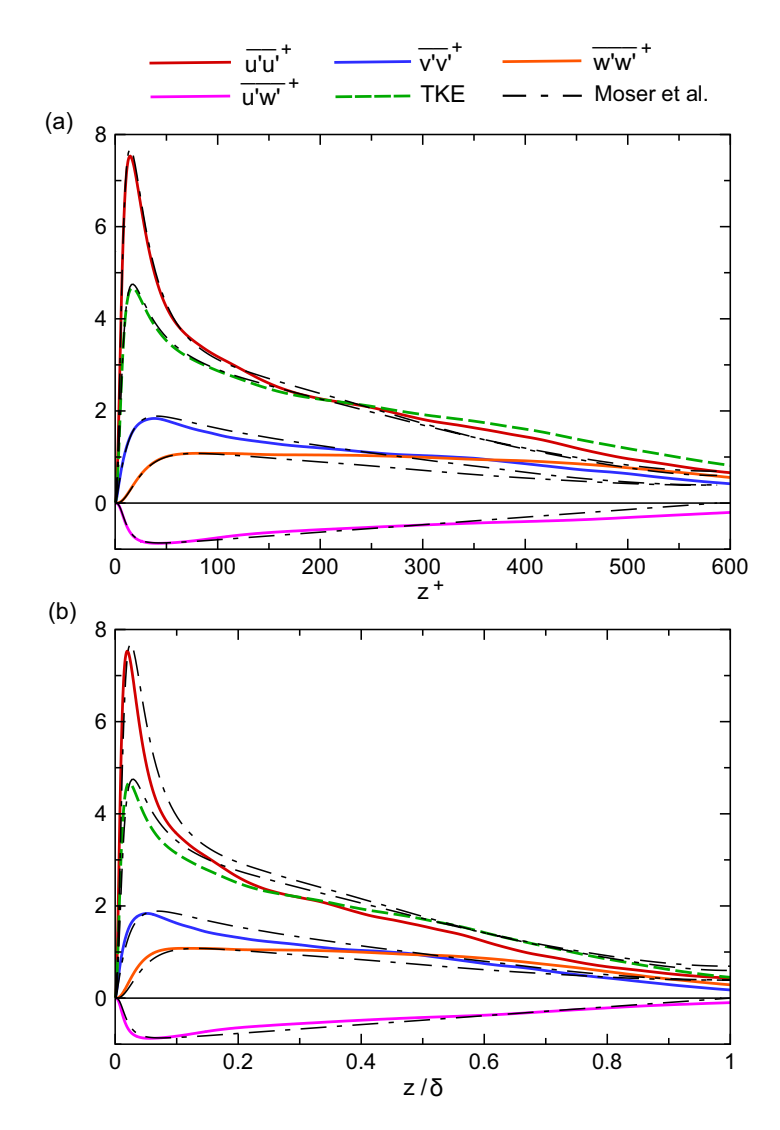


FIG. 8. Wall-normal distribution of wall-scaled Reynolds stresses at $x = 17H \approx 7.3\lambda_w$ presented in (a) viscous scale and (b) boundary layer scale. Dashed line represents the turbulence kinetic energy $0.5\overline{u_i'u_i'}^+$. Dot-dashed line represents DNS data for a channel flow obtained by Moser *et al.* [23] for $\text{Re}_{\tau}(\equiv u_{\tau}\delta/\nu) = 590$.

C. Turbulence properties: Kinetic energy budget

In this section, we further explore the wake relaxation in terms of the TKE budget. Specifically, we compare TKE statistics with the statistics of a planar mixing layer, ZPG turbulent boundary layers, and separated boundary layers of shorter bubbles. We further identify distinct characteristics of the wake relaxation statistics in the near-wall and far-wall regions. At the end of this section, key observations are summarized along with physical insights gained from the flow statistics in this paper.

1. Near-wall distribution of TKE

In Fig. 10, we show the standard, wall-scaled TKE budget terms of in the viscous-wall region for the same four streamwise locations as chosen previously in Sec. III B. The budget of TKE

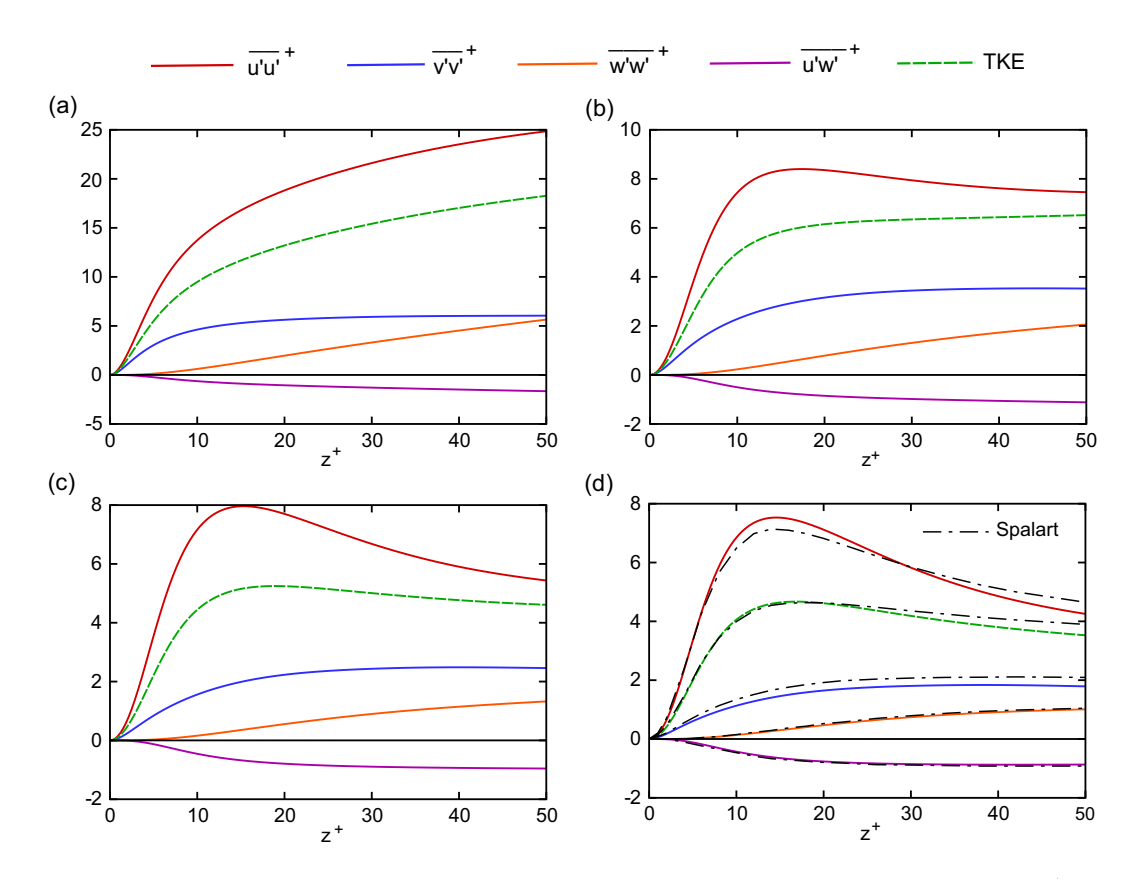


FIG. 9. Wall-normal distribution of wall-scaled Reynolds stresses presented over viscous-wall scale z^+ for the viscous-wall region. Dashed line represents the turbulence kinetic energy $0.5\overline{u_i'u_i'}^+$. (a) $x = 7H \approx 3\lambda_w$, (b) $x = 9H \approx 3.9\lambda_w$, (c) $x = 11H \approx 4.3\lambda_w$, and (d) $x = 17H \approx 7.3\lambda_w$. Dot-dashed line in (d) is Spalart [22] for Re_{\theta} = 1410. Note the different vertical axis limits across panels.

 $(0.5\partial\overline{u_i'u_i'}/\partial t)$, comprising terms pertaining to advection $-\overline{u_j}(\overline{u_i'u_i'})_j/2$, turbulent diffusion (transport) $-(u_i'u_i'u_j')_j/2$, production $-u_i'u_j'(\overline{u_i})_j$, pressure work $-(\overline{u_i'p'})_i/\rho_0$, viscous diffusion $v\nabla^2u_i'u_i'/2$, and dissipation $-v(\overline{u_i'})_j(u_i')_j$, where $(\cdots)_j \equiv \partial(\cdots)/\partial x_j$, is expressed as follows:

$$\frac{1}{2}\frac{\partial\overline{u_i'u_i'}}{\partial t} = -\frac{1}{2}\overline{u_j}(\overline{u_i'u_i'})_j - \frac{1}{2}(\overline{u_i'u_i'u_j'})_j - \overline{u_i'u_j'}(\overline{u_i})_j - \frac{1}{\rho_0}(\overline{u_i'p'})_i + \frac{\nu}{2}\nabla^2\overline{u_i'u_i'} - \nu\overline{(u_i')_j(u_i')_j}.$$
 (2)

For the early turbulent cloud formation stage [Fig. 10(a), measured at a downstream distance of $1.4l_b$ from the reattachment point], the viscous diffusion and dissipation terms are significantly larger than the production term in the viscous sublayer ($z^+ < 5$). The budget term distributions appear to be similar to those reported in Alam and Sandham's short bubble measured at about $1l_b$ downstream from the reattachment point (see their Fig. 15(b), in Ref. [3]).

The budget term distributions of the intermediate turbulent cloud formation stage [Fig. 10(b)] are similar to those of the late turbulent cloud formation and developing turbulent boundary layer stages [Figs. 10(c) and 10(d)]. This is consistent with trends observed in the Reynolds stresses in the viscous-wall region discussed in the previous section (see Fig. 9). For the late turbulent cloud formation and developing turbulent boundary layer stages [Figs. 10(c) and 10(d)], the distributions are essentially the same, which suggests that the near-wall boundary layer has relaxed to that of a

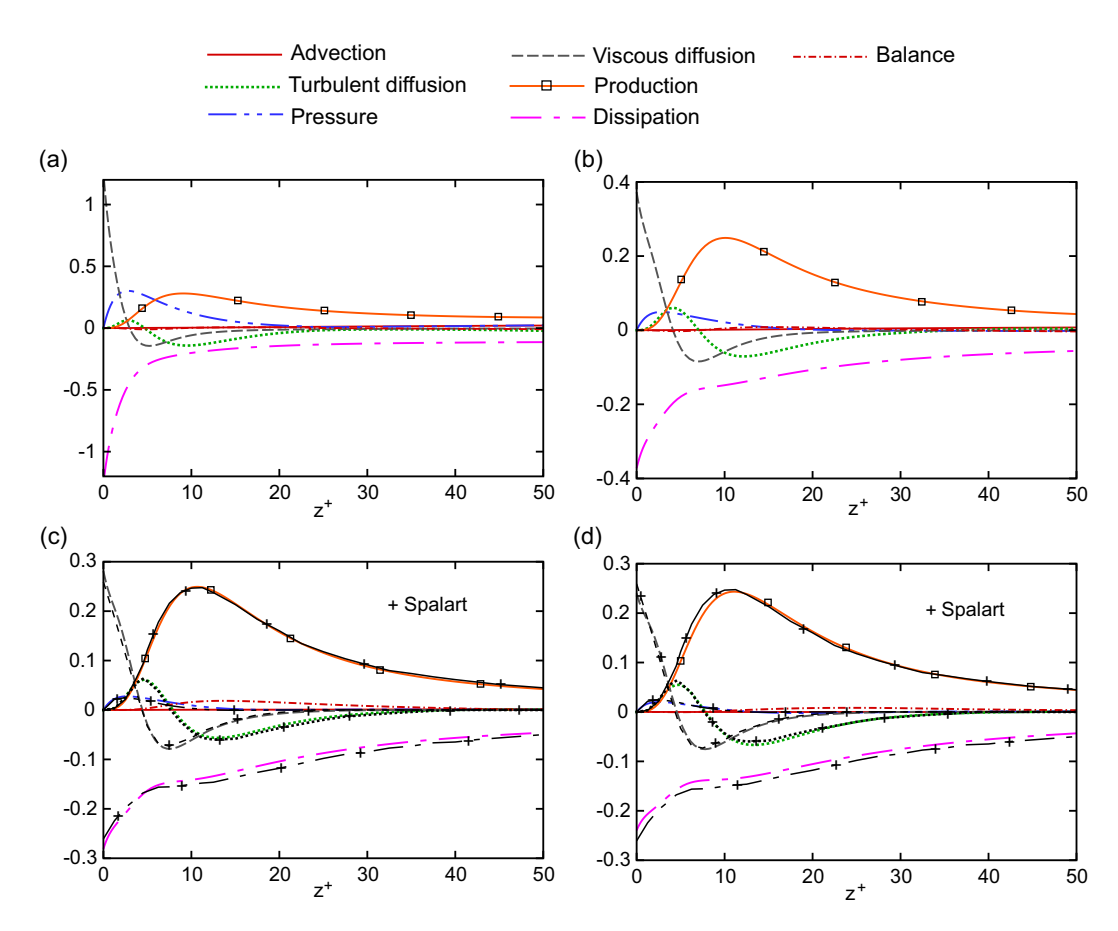


FIG. 10. Wall-scaled TKE budget terms in the viscous-wall region. (a) $x = 7H \approx 3\lambda_w$, (b) $x = 9H \approx 3.9\lambda_w$, (c) $x = 11H \approx 4.3\lambda_w$, and (d) $x = 17H \approx 7.3\lambda_w$. In all cases the advection term is essentially zero. Black lines with + (with the same line styles defined in the legend) in (c) and (d) are Spalart [22] for $Re_\theta = 1410$. Positive values (gain) and negative values (loss). Note the different vertical axis limits across panels.

ZPG turbulent boundary layer by x = 11H. In Fig. 10, the Spalart boundary layer data ($Re_{\theta} = 1410$) is also plotted for comparison. From the comparison, we conclude that the present LES simulation slightly underestimates the dissipation because we do not resolve all scales and Spalart's DNS does. Because of this underestimation, the budget balance [sum of all the budget terms on the right-hand side of Eq. (2)] yields slightly positive values. Despite this, the present results compare quite well with the Spalart benchmark. The underprediction of dissipation can be attributed to an accumulated effect of spectral filtering applied every time step during the long-time integration.

2. Far-wall distribution of TKE

Figure 11 shows the TKE budget term distributions away from the wall. The budget terms are scaled by the boundary layer scales, i.e., the local free-stream velocity $u_{\infty} - c$ and the boundary layer thickness δ , following Spalart's presentation. While the budget is not balanced as well as in the near wall region, we find that the comparison with DNS data is still reasonable, as elaborated below.

The early and intermediate turbulent cloud formation stages show qualitatively the same budget term distributions [Figs. 11(a) and 11(b)]. Antisymmetric shapes of the turbulent diffusion, pressure transport, and balance terms about $z/\delta \approx 0.5$, and roughly symmetric shape of the production and

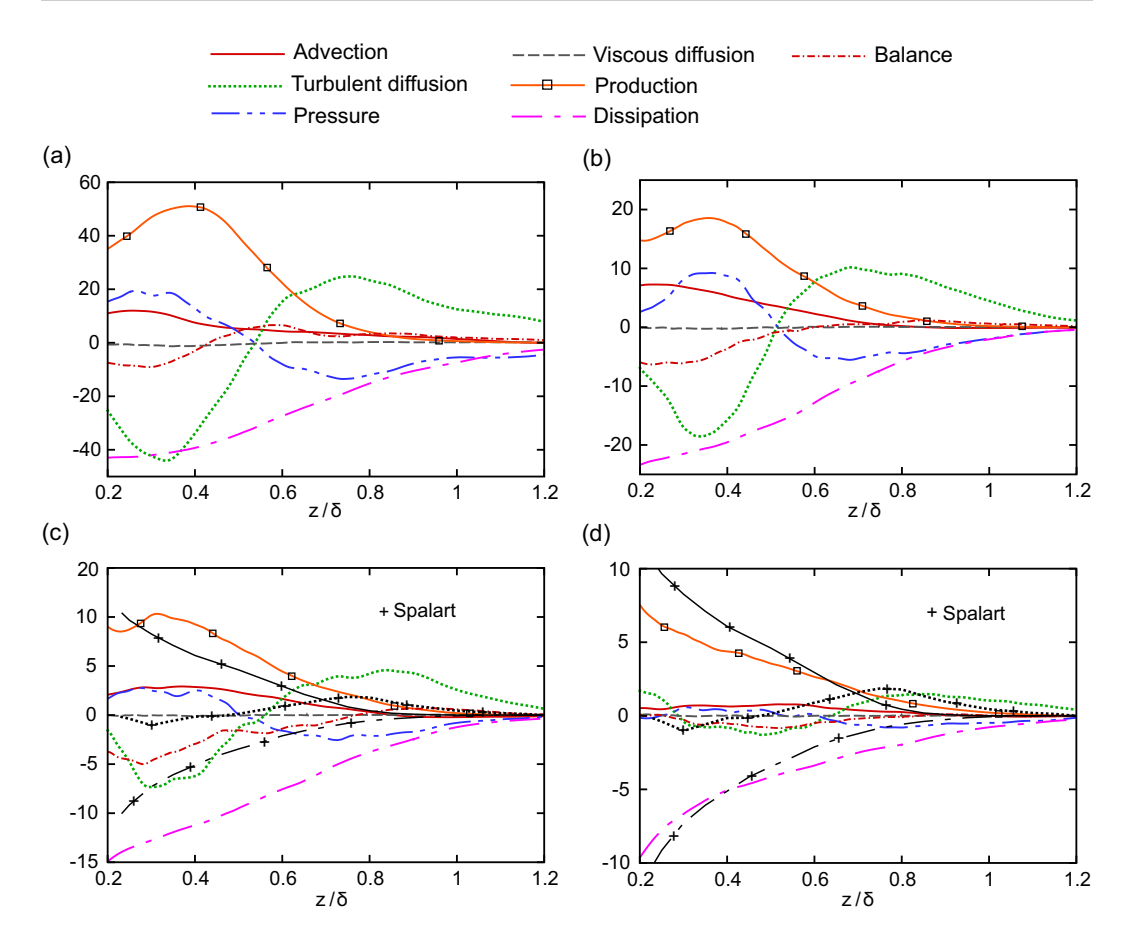


FIG. 11. Boundary-layer-scaled turbulent kinetic energy budget terms away from the wall. (a) $x = 7H \approx 3\lambda_w$, (b) $x = 9H \approx 3.9\lambda_w$, (c) $x = 11H \approx 4.3\lambda_w$, and (d) $x = 17H \approx 7.3\lambda_w$. Black lines with + (production, dissipation, and turbulent diffusion, with the same line styles defined in the legend) in (c) and (d) are Spalart [22] for Re_{\theta} = 1410. Positive values (gain) and negative values (loss). Note the different vertical axis limits across panels.

dissipation terms about $z/\delta \approx 0.4$ are structurally similar to those in the upper half of a self-similar mixing layer obtained by Rogers and Moser [25] [see their Fig. 21(e)]. Similar mixing-layer features are also found in the studies of Alam and Sandham's short bubbles (see Fig. 15(b) in Ref. [3]) and Le *et al.*'s backward-facing step (see Fig. 25 for y/h > 0.7 in Ref. [14]). Clearly, mixing-layer-like characteristics play a defining role in the early stages of the wake relaxation.

In the late turbulent cloud formation and the developing turbulent boundary layer stages [Figs. 11(c) and 11(d)], only three dominant budget terms (production, dissipation, and turbulent diffusion) of the Spalart boundary layer are plotted for comparison. In the late turbulent cloud formation stage [Fig. 11(c)], the budget terms are much larger than those of the Spalart boundary layer but still exhibit the character of a mixing layer. In the developing turbulent boundary layer stage [Fig. 11(d)], the budget distributions are qualitatively similar to the Spalart boundary layer, with a slight nonvanishing balance. Larger magnitudes of the budget terms are observed in the upper portion of the boundary layer ($z/\delta > 0.8$); their decay in the wall-normal direction is much slower as compared to the Spalart boundary layer. The significant turbulent diffusion around the outer edge of boundary layer [observed in Figs. 11(c) and 11(d)] effectively contributes to transport the Reynolds stresses toward the edge of the boundary layer, which thickens the boundary layer. Note

that the dissipation rate is much smaller in the outer layer compared to that in the viscous sublayer (see Fig. 10); such nonnegligible budget terms suggest that the turbulence away from the wall, i.e., the wake turbulence, is still energetic and not yet sufficiently dissipated to recover a ZPG turbulent boundary layer at the end of the domain.

3. Summary

To summarize, it is reconfirmed that the BBL, produced by a long separation bubble under an ISW, relaxes from the mixing-layer-like flow to a flat plate turbulent boundary layer is also described by Alam and Sandham's aerodynamic short separation bubbles (see Fig. 15 in Ref. [3]). This is consistent with the observations based on the mean flow properties and Reynolds stresses in the previous sections. In particular, the relaxation of energy budgets to those of the Spalart boundary layer is remarkably evident in the viscous-wall region, where the energy budget is relaxed at $x \approx 11H$ ($\approx 5\lambda_w$) that corresponds to about $3l_b$ downstream from the mean reattachment point. The relaxation of energy budget in the far-wall region is rather slow compared to that in the viscous-wall region due to the vigorous, mixing-layer-like turbulence occurring at some distance away from the wall; and, consequently, the relaxation is slower far away from the wall and faster near the wall than that of the mean velocity profile (15H).

This observation has an important implication in coastal application in the sense that the memory of ISW-induced APG can persist over a longer distance downstream, which cannot be predicted solely from the relaxation of mean flow profile to that of a ZPG turbulent boundary layer. Faster relaxation near the wall is also manifested in the streamwise turbulence energy spectra given in Fig. 15(a) in Part I, where the characteristic slope of turbulent energy spectra becomes larger than -5/3 (about -7/3) closer to the wall. Such a layer-dependent, nonuniform relaxation character is commonly observed in experimental studies of backward-facing step (e.g., Bradshaw and Wong [26] and Jovic [27] among others) and, therefore, is a common phenomenon in reattached turbulent flows.

IV. DISCUSSION

Given the energetic coherent structures and high turbulence intensities observed in the simulation reported here, questions that naturally arise are whether the ISW-induced turbulent BBL is capable of resuspending sediment and how this laboratory-scale study compares to field observations in this context. In diagnosing the potential for bottom sediment resuspension, we examine an instantaneous bed stress distribution rather than its statistical average because time averaging smooths out strong spatiotemporally local bottom shear stress events and, as such, underestimates the magnitude of shear stress. In addition to the bed shear stress, near-bed turbulence intensity plays an important role in lifting the mobilized particles away from the bed.

Figure 12 shows a typical, instantaneous, spanwise-averaged, streamwise bed shear stress distribution along the bottom, where the shear stress is nondimensionalized by the constant characteristic dynamic pressure $\rho_0 c_{w0}^2/2$. From the figure it is clear that the maximum local stress is found near the flow reattachment region ($x/H \approx 3.3$), and the stress magnitude is strikingly large, roughly double the stress underneath the wave trough. The amplitudes of the stress fluctuations decrease and connect to the turbulent region where the amplitudes are much smaller but randomly fluctuating at higher frequencies. It is also clear that the fluctuation signature near the initial vortex shedding region has short wavelengths (linked to the spacing of coherent vortices) which increase in the subsequent vortex pairing and merger region.

The potential for sediment mobilization is measured by the standard calculation in terms of the Shields parameter θ_s , as defined by

$$\theta_s = \frac{\tau_b}{(\rho_* - \rho_b)gd},\tag{3}$$

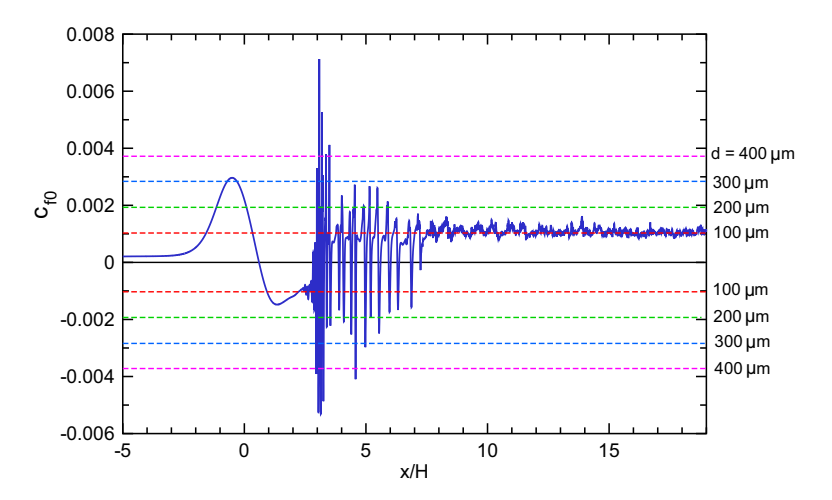


FIG. 12. Instantaneous spanwise-averaged bed shear stress coefficient $c_{f0} = 2\tau_b/\rho_0 c_{w0}^2$ along the streamwise axis, together with critical shear stress for sediment mobilization for grain sizes 100, 200, 300, and 400 μ m in dashed lines.

where ρ_* is the grain density, ρ_b is the bottom water density, and d is the grain diameter. The critical Shields parameter θ_{sc} is given by the empirical correlation [28]:

$$\theta_{sc} = \frac{0.3}{1 + 1.2D_*} + 0.055(1 - e^{-0.02D_*}),\tag{4}$$

where the dimensionless grain size is given by

$$D_* = \left[\frac{g(\rho_*/\rho_b - 1)}{v^2} \right]^{\frac{1}{3}} d. \tag{5}$$

We choose $\rho_*=2650~{\rm kg/m^3}$ representing the density of quartz. The typical grain size is a few to several hundreds μm in the coastal ocean. For instance, for the large ISW site at the western Portuguese midshelf, the sand grain size ranges from 100 to 400 μm with a median of 214 μm [29]. For the upper continental slope in the South China Sea, the major spectral peaks of the grain size are 200, 300, and 400 μm [30].

Given these materials, the critical bed shear stresses are calculated for a series of the grain sizes $100,\,200,\,300,\,$ and $400\,\mu m,\,$ as indicated by the horizontal dashed lines in Fig. 12. The effect of surface roughness on the bed shear stress is neglected. Per Fig. 12, the medium-size grain can be routinely mobilized in the high stress region underneath the wave trough. Near the reattachment region, the large local shear stress can easily mobilize even the coarse grains. The subsequent vortex ejection can possibly suspend particles by the large local upwelling velocity of the merged vortices and the turbulent clouds. Further resuspension follows throughout the turbulent boundary layer which develops thereafter. In the developing turbulent boundary layer, the fine grains or neutrally buoyant particles can be routinely mobilized.

Figure 13(a) shows the wall-normal turbulence strength $\sqrt{w'^2}$ in the viscous-wall region at x/H=4 (near the flow reattachment point), x/H=9 (intermediate stage of the turbulent cloud formation), and x/H=17 (developing turbulent boundary layer). Values of the Stokes particle settling velocity $w_s=(\rho_*/\rho_b-1)gd^2/18\nu$ for different grain sizes (100 μ m $\leq d \leq 400 \ \mu$ m) are also included. For sediment resuspension to occur, the mobilized near-bed particles need to be transported away from the bed by the driving (drag) force induced by the wall-normal turbulence fluctuation [31]. Aghsaee and Boegman [32] showed in a series of laboratory experiments where, in addition to sufficiently large bed shear stresses, sufficiently large vertical velocities are required

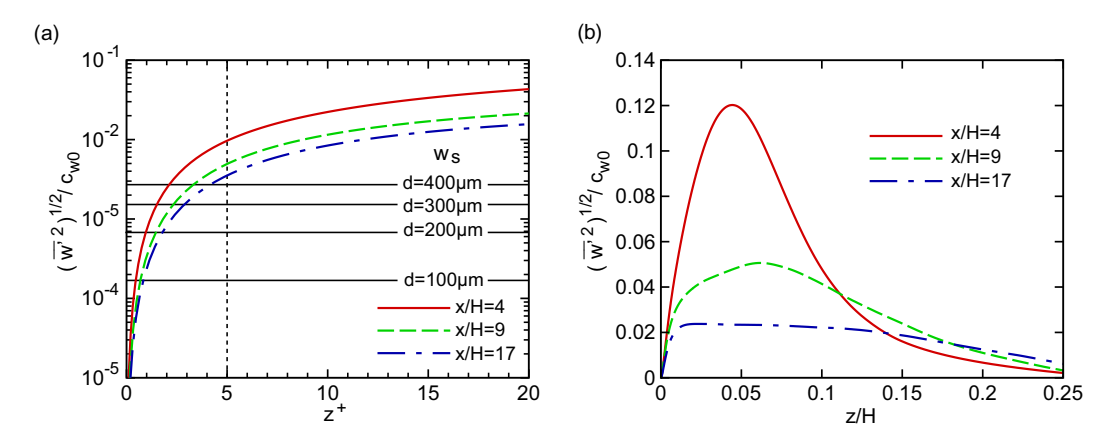


FIG. 13. (a) Wall-normal turbulence intensities $\sqrt{w^2}/c_{w0}$ as functions of wall-scaled wall-normal coordinate z^+ at different streamwise locations $x/H = \{4, 9, 17\}$ together with the particle settling velocities w_s (horizontal solid lines) for particle diameters $d=100, 200, 300, \text{ and } 400 \ \mu\text{m}$. The vertical axis is log scaled. The region $z^+ < 5$, as indicated by the vertical dashed line, is the viscous sublayer. (b) The same quantities $(\sqrt{w'^2}/c_{w0})$ are presented in linear scale as functions of the global wall-normal coordinate z/H.

for sediment resuspension to occur underneath an ISW. In Fig. 13(a), it is clear that the values of $\sqrt{w'^2}$ become larger than the particle settling velocities inside the viscous sublayer $(z^+ < 5)$ in all three streamwise locations. The values of $\sqrt{w'^2}$ consistently increase outside the viscous sublayer. As shown in Fig. 13(b), in particular, the $\sqrt{w'^2}$ value near the reattachment point is largest $(\approx 0.12c_{w0}$ at x/H = 4 and $z/H \approx 0.05$), where vigorous particle resuspension is likely to occur. In the same figure, noting that even the developing turbulent boundary layer downstream (x/H = 17) induces sufficiently large values of $\sqrt{w'^2}$ [$\approx 0.02c_{w0} \sim O(10w_s$ to $100w_s$)] to suspend the particles, we expect that any potentially formed layer of suspended particles (nepheloid layer) can be sustained far downstream of the ISW.

The observational studies of Quaresma et al. [29] and Zulberti et al. [33] reported the highest levels of turbidity, presumably associated with the most intense turbulence in the ISW-induced BBL, to occur immediately beneath the wave trough. This contrasts with the present case and laboratory-scale studies conducted by Carr and Davies [34] and Aghsaee and Boegman [32], who found active bottom turbulence occurring in the downstream side of the wave. How to compromise the field observations with such laboratory-scale investigations is an open question. One potential conjecture may be motivated by the fact that the BBL driven by background currents in the actual ocean is already highly turbulent, unlike the idealized Blasius boundary layer associated with the background current in this study. As such, although the FPG in the front shoulder of the wave [35] may weakly suppress any near-bed background turbulence, this turbulence can be rapidly and significantly amplified as soon as it experiences an APG, initially at the wave trough and then further downstream under the wave [36]. Interaction between the wave induced current and a local irregular topography can excite a jet-roll instability as discovered by Harnanan et al. [37], which may be another potential conjecture for the active bottom turbulence to occur underneath the wave trough. Additional simulations, at nontrivial computational cost, with a background current supporting a preexisting turbulent BBL with and/or without local topography perturbations would be needed to explore this question in a computational context.

Additionally, the observational findings of Bogucki *et al.* [38] actually report elevated beam-*C*-attenuation (resuspension of bottom particulates) to be offset more downstream with respect to the wave trough, as compared to what Quaresma *et al.* and Zulberti *et al.* have observed. The particular

downstream offset, as inferred at least from low temporal resolution thermistor measurements, appears to be between one to two ISW wavelengths, which is still quite smaller when compared to the present study. Further work is needed, nevertheless, to interpret the differences between Bogucki *et al.* and the above discussed observational studies in this regard.

V. CONCLUDING REMARKS

The wake relaxation behind an ISW induced long separation bubble is analyzed using turbulence statistics. The long, high-aspect-ratio laminar separation bubble is induced by a high-amplitude, laboratory-scale ISW propagating against an oncoming barotropic current over a smooth bottom in uniform-depth water. Through comparisons with various canonical flows, we have characterized the relaxation of the mean flow and turbulent fluctuations in near- and far-wall regions and have identified the similarities and differences of the wake relaxation character as compared to lower aspect ratio, aerodynamic short bubbles.

The early stage of downstream evolution of the turbulent wake has a similar statistical character to that of a canonical, self-similar turbulent mixing layer of Rogers and Moser [25]. The existence of such a mixing layer signature is not only a characteristic of the near-bed wake, but also a notable feature of originally separated, and subsequently reattached turbulent flows. Following the turbulent cloud formation stage, at approximately 15 water column depths downstream from the wave trough, which also corresponds to five bubble lengths from the bubble trailing edge, the mixing-layer-like structure is (though not completely) relaxed, and the mean streamwise velocity profile approaches that of a spatially developing ZPG flat plate turbulent boundary layer. This wake relaxation process is qualitatively similar to the case of Alam and Sandham's forced short separation bubble. For Alam and Sandham's case, the relaxation distance normalized by the bubble length is 6 which is longer than our case because of their stronger APG.

At the developing turbulent boundary layer state, the second-order statistics compare very well with those of Spalart's ZPG turbulent boundary layer [22] in the viscous-wall region. The pronounced Reynolds stresses in the outer layer gives a clear distinction from ZPG turbulent boundary layers, attributed to the memory of the wave-induced APG, as driven by the vigorous wake turbulence generated through vortex shedding, pairing and merger, breakup and subsequent formation of the turbulent clouds. The wall-normal distributions of Reynolds stresses rather resemble those of Moser *et al.*'s channel flow [23] because of the persistent, promoted wake turbulence in the far-wall region.

The wake relaxation of the turbulent fluctuations is thus faster near the wall than in the farwall region because of the energetic turbulence occurring at a particular vertical offset from the highly dissipative viscous-wall region, where the corresponding energy spectra have a slope greater than -5/3. The TKE budget has relaxed in the viscous-wall region at 11 water column depths downstream from the wave trough or three bubble lengths from the trailing edge of the separation bubble. Instead, the TKE relaxation in the far-wall region is slower and the turbulence intensity there is not negligible even at the end of the computational domain, in contrasting to the faster relaxation of the mean flow (15 water column depths). This observation suggests that the memory of the wave-induced APG persists for a longer distance, say at least 18 water column depths (\sim 8 wavelengths) in the region far away from the ocean bed (\sim 0.1 to 0.3 water column depth), than what can be predicted from the mean flow measurement.

Wake relaxation from a mixing-layer-like state to a flat plate boundary layer with a pronounced rate of equilibrium, i.e., shorter relaxation distance, near the wall is generally a common phenomenon for reattached turbulent flows. Beside the Reynolds number, the rate of wake relaxation seems to depend primarily on the strength and spatial distribution of APG, features specific to the particular separated flow, as well as on the specification of upstream disturbances and forcing (e.g., Refs. [5,26,39]); these flow specifications are strong functions of wave amplitude and background current. Further computational process study is needed to fully understand the dependence of the rate of wake relaxation on these controlling parameters.

For our ISW-induced long bubble, the flow undergoes transition at a nonnegligible downstream distance from the reattachment point of the initially separated flow. This is in contrast to the cases of aerodynamic short bubbles, for which the transition occurs near the reattachment point. The physical mechanism that drives such a discrepancy is not known and is recommended for future investigations. Here three key control parameters are conjectured to play a significant role, including (a) strength of APG, (b) upstream forcing, and (c) domain width. Typically, the aerodynamic short bubbles are driven by a strong APG and forced by upstream disturbances, effects that are not applicable in the case of our long bubble. The narrow domain size used for this study may have suppressed the centrifugal instability mode [40] which is expected to accelerate the transition.

As part of an effort to gain physical insights into environmental impacts of such a long-residing memory of wave-induced APG, we have examined the bed stresses and the near-bed, wall-normal turbulent fluctuation field for potential sediment resuspension. When an ISW possessing a large amplitude encounters relatively large oncoming barotropic current, the sediment and particulate matter can be mobilized and resuspended from the ocean bed due to large, fluctuating bed stresses exerted by a train of coherent vortices that are continually shed from the separation bubble, followed by an intense turbulent wake. Such a suspended (nepheloid) layer of particles, i.e., a signature of wave-induced APG, is expected to persist at least several wavelengths, say 15 water column depths, in the wake of ISW, in which a pronounced turbulence production across the thick boundary layer is expected to enhance the suspension. Comparison between field observations and laboratory-scale process studies is inconclusive, as the sediment resuspension is observed to be predominant beneath the wave trough [33] for the former case in contrast to the wave downstream side for the latter case. Future work may address this disparity through numerical simulations under freely evolving upstream conditions with pre-existing turbulence combined with local bottom topography perturbations.

ACKNOWLEDGMENTS

The support of Office of Naval Research Grant No. N00014-11-1-0511 and National Science Foundation OCE CAREER Grant No. 0845558 are gratefully acknowledged. The second author acknowledges additional support by National Science Foundation OCE Grant No. 1634257. The authors thank Professor L. G. Redekopp for numerous inspiring conversations on this problem. Additional insightful discussions with Professor J. A. Domaradzki are also acknowledged. High-performance computing resources were provided through the U.S. Department of Defense High Performance Computing Open Resource Systems. G.B.J. is grateful for support from the Air Force Office of Scientific Research under Grant No. FA9550-16-1-0392.

^[1] V. Theofilis, Global linear instability, Annu. Rev. Fluid Mech. 43, 319 (2011).

^[2] R. R. Kerswell, Elliptic instability, Annu. Rev. Fluid Mech. 34, 83 (2002).

^[3] M. Alam and N. D. Sandham, Direct numerical simulation for 'short' laminar separation bubbles with turbulent reattachment, J. Fluid Mech. 403, 223 (2000).

^[4] S. S. Diwan and O. N. Ramesh, On the origin of the inflectional instability of a laminar separation bubble, J. Fluid Mech. **629**, 263 (2009).

^[5] O. Marxen and D. S. Henningson, The effect of small-amplitude convective disturbances on the size and bursting of a laminar separation bubble, J. Fluid Mech. 671, 1 (2011).

^[6] J. H. Watmuff, Evolution of a wave packet into vortex loops in a laminar separation bubble, J. Fluid Mech. **397**, 119 (1999).

^[7] T. Michelis, S. Yarusevych, and M. Kotsonis, On the origin of spanwise vortex deformations in laminar separation bubbles, J. Fluid Mech. **841**, 81 (2018).

^[8] P. Huerre and P. A. Monkewitz, Local and global instabilities in spatially developing flows, Annu. Rev. Fluid Mech. **22**, 473 (1990).

- [9] L. E. Jones, R. D. Sandberg, and N. D. Sandham, Direct numerical simulations of forced and unforced separation bubbles on an airfoil at incidence, J. Fluid Mech. 602, 175 (2008).
- [10] O. Marxen, M. Lang, and U. Rist, Vortex formation and vortex breakup in a laminar separation bubble, J. Fluid Mech. 728, 58 (2013).
- [11] P. R. Spalart and M. K. Strelets, Mechanisms of transition and heat transfer in a separation bubble, J. Fluid Mech. 403, 329 (2000).
- [12] M. Dunphy, C. Subich, and M. Stastna, Spectral methods for internal waves: Indistinguishable density profiles and double-humped solitary waves, Nonlin. Proc. Geophys. 18, 351 (2011).
- [13] P. J. Diamessis and L. G. Redekopp, Numerical investigation of solitary intenal wave-induced global instability in shallow water benthic boundary layers, J. Phys. Oceanogr. 36, 784 (2006).
- [14] H. Le, P. Moin, and J. Kim, Direct numerical simulation of turbulent flow over a backward-facing step, J. Fluid Mech. 330, 349 (1997).
- [15] F. M. White, Fluid Mechanics (McGraw-Hill Education, New York, 2016).
- [16] D. E. Coles, The turbulent boundary layer in a compressible fluid, Technical Report No. R-403-PR, The RAND Corporation, 1962.
- [17] P. A. Monkewitz, K. A. Chauhan, and H. M. Nagib, Comparison of mean flow similarity laws in zero pressure gradient turbulent boundary layers, Phys. Fluids 20, 105102 (2008).
- [18] H. Ludwieg and W. Tillmann, Investigation of the wall-shearing stress in turbulent boundary layers, Tech. Rep. No. TM1285, National Advisory Committee for Aeronautics, 1950.
- [19] Y. Nagano, M. Tagawa, and T. Houra, Effects of adverse pressure gradients on mean flows and turbulence statistics in a boundary layer, Int. J. Heat Fluid Flow 19, 563 (1998).
- [20] J. P. Monty, Z. Harun, and I. Marusic, A parametric study of adverse pressure gradient turbulent boundary layers, Int. J. Heat Fluid Flow 32, 575 (2011).
- [21] J. Murlis, H. M. Tsai, and P. Bradshaw, The structure of turbulent boundary layers at low Reynolds numbers, J. Fluid Mech. 122, 13 (1982).
- [22] F. R. Spalart, Direct simulation of a turbulent bounday layer up to $R_{\theta} = 1410$, J. Fluid Mech. 187, 61 (1988).
- [23] R. D. Moser, J. Kim, and N. N. Mansour, Direct numerical simulation of turublent channel flow up to $Re_{\tau} = 590$, Phys. Fluids 11, 943 (1999).
- [24] S. B. Pope, *Turbulent Flows* (Cambridge University Press, Cambridge, UK, 2000).
- [25] M. M. Rogers and R. D. Moser, Direct simulation of a self-similar turbulent mixing layer, Phys. Fluids 6, 903 (1994).
- [26] P. Bradshaw and F. Y. F. Wong, The reattachment and relaxation of a turbulent shear layer, J. Fluid Mech. **52**, 112 (1972).
- [27] S. Jovic, An experimental study of a separated/reattached flow behind a backward-facing step. $Re_h = 37,000$, Technical Memorandum No. TM110384, National Aeronautics and Space Administration, Ames Research Center, Moffett Field, California, 1996.
- [28] R. L. Soulsby, Dynamics of Marine Sands (R. Soulsby and Thomas Telford Services Limited, London, 1997)
- [29] L. S. Quaresma, J. Votorino, A. Oliviera, and J. da Silva, Evidence of sediment resuspension by nonlinear internal waves of the western Portuguese mid-shelf, Mar. Geol. **246**, 123 (2007).
- [30] D. B. Reeder, B. B. Ma, and Y. J. Yang, Very large subaqueous sand dunes on the upper continental slope in the South China Sea generated by episodic, shoaling deep-water internal solitary waves, Mar. Geol. 279, 12 (2010).
- [31] L. C. Van Rijn, *Principles of Sediment Trasnport in Rivers, Estuaries and Coastal Seas* (Aqua, Naples, FL, 1993).
- [32] P. Aghsaee and L. Boegman, Experimental investigation of sediment resuspension beneath internal solitary waves of depression, J. Geophys. Res. Oceans 120, 3301 (2015).
- [33] A. Zulberti, N. L. Jones, and G. N. Ivey, Observations of enhanced sediment transport by nonlinear internal waves, Geophysical Research Letters 47, e2020GL088499 (2015)

- [34] M. Carr and P. A. Davies, Boundary layer flow beneath an internal solitary wave of elevation, Phys. Fluids **22**, 026601 (2010).
- [35] U. Piomelli, E. Balaras, and A. Pascarelli, Turbulent structures in accelerating boundary layers, J. Turbul. 1, N1 (2000).
- [36] J. H. Lee, Large-scale motions in turbulent boundary layers subjected to adverse pressure gradients, J. Fluid Mech. 810, 323 (2017).
- [37] S. Harnanan, N. Soontiens, and M. Stastna, Internal wave boundary layer interaction: A novel instability over broad topography, Phys. Fluids 27, 016605 (2015).
- [38] D. J. Bogucki, L. G. Redekopp, and J. Barth, Internal solitary waves in the Coastal Mixing and Optics 1996 Experiment: Multimodal structure and resuspension, J. Geophys. Res. 110, C02024 (2005).
- [39] O. Marxen, M. Lang, U. Rist, O. Levin, and D. S. Henningson, Mechanisms for spatial steady threedimensional disturbance growth in a non-parallel and separating boundary layer, J. Fluid Mech. 634, 165 (2009).
- [40] D. Rodríguez, E. M. Gennaro, and M. P. Juniper, The two classes of primary modal instability in laminar separation bubbles, J. Fluid Mech. 734, R4 (2013).